

Green synthesis and characterization of mixed-phase Fe₂O₃ nanorods as a novel magnetically recoverable heterogeneous catalyst for Biginelli synthesis

Dnyaneshwar Sanap^{a, b, *}, Lata Avhad^c, Suresh Ghotekar^{d, *}, Nitin D. Gaikwad^{a, *}

^a Department of Chemistry, Organic Chemistry Research Centre, K.R.T. Arts, B.H. Commerce, and A.M. Science College, Savitribai Phule Pune University Pune, Gangapur Road, Nashik, 422002 Maharashtra, India

^b Department of Chemistry, Organic Chemistry Research Centre, G.M.D. Arts B.W. Commerce and Science College Sttnar, Savitribai Phule Pune University, Pune 422103, Maharashtra, India

^c Department of Chemistry, Arts, Commerce and Science College Dindori, Savitribai Phule Pune University Pune, Nashik 422202, Maharashtra, India

^d Department of Chemistry, Smt. Devkiba Mohansinhji Chauhan College of Commerce & Science, University of Mumbai, Silvassa, Dadra and Nagar Haveli (UT), 396230 India

ARTICLE INFO

Article history:

Received 8 January 2023

Received in revised form 18 February 2023

Accepted 24 February 2023

Keywords:

Green synthesis

Biginelli reaction

Fe₂O₃ NRs

Characterization

Heterogeneous catalysis

ABSTRACT

For the first time, mixed-phase (Hematite and Maghemite) magnetic Fe₂O₃ nanorods were successfully biosynthesized by sol-gel auto-combustion method using the 1:1 mixture of *Eucalyptus citriodora* and *Murraya koenigii* leaf extract as a capping agent, and its catalytic effect on synthesis of 6-(chloromethyl)-1,2,3,4-tetrahydro-2-pyrimidinone (THPMs) derivatives were investigated. Further, the phase formation, surface topography, and crystallinity of biosynthesized Fe₂O₃ nanorods (NRs) were explored using powder XRD (X-Ray Diffraction), UVDRS (UV-Visible Reflectance Spectroscopy), FTIR (Fourier Transform Infrared Spectroscopy), FESEM (Field Emission Scanning Electron Microscopy), EDX (Energy Dispersive X-Ray), and VSM (Vibrating Sample Magnetometry). Furthermore, the catalytic activity of biosynthesized Fe₂O₃ NRs (C1, C2, and C3) was examined for one-pot synthesis of ethyl 6-(chloromethyl)-1,2,3,4-tetrahydro-2-oxo-4-arylpyrimidine-5-carboxylate via Biginelli reaction. To achieve high yields (93–99 %) of 6-(chloromethyl)-1,2,3,4-tetrahydro-2-pyrimidinone derivatives, this heterogeneous catalytic method is used with a wide range of aromatic aldehydes within a minimum reaction time, simple reaction work-up, and easily recoverable catalyst by an external magnet. The recovered catalyst is then employed for five successive cycles without non-noticeable loss of catalytic activity. We believe that this protocol presents a broad scope for Biginelli reaction through green produced and magnetically separable heterogeneous catalysts.

© 20XX

1. Introduction

Advanced nanotechnology has produced a plethora of research opportunities for science and engineering in recent years [1–5]. Applications of metal oxide-containing nanoparticles (NPs) can be found in electronics, biology, chemistry, physics, and medicine [6–8]. The large surface-area-to-volume ratio of NPs allows them to perform novel functions in magnetism, biology, optics, sensing, and catalysis [9–12]. In contrast to their bulk substance, the iron-containing NPs reveal special characteristics [13–16]. Iron oxide NPs are well known for their innumerable uses as a pigment [17], magnetic material [18], sensors [19], and catalysts [20–23]. Additionally, iron oxide NPs are employed in technical applications, bio-diagnosis, and bio-medication. There are many different polymorphs of iron oxide NPs, including hematite (α -Fe₂O₃), maghemite (γ -Fe₂O₃), magnetite (Fe₃O₄), and goethite (FeO) (OH) [24,25].

Nano-catalysts can allow facile, high-purity product separation from reaction mixtures, and catalysts can also be recycled for several cycles with the same catalytic performance [26,27]. As a result, the NPs are an impressive replacement for homogeneous catalysis to enable high product yields at rapid reaction rates [28,29]. Recently, Fe₂O₃ NPs have been investigated as effective recyclable catalysts for C-C cross-coupling [30], Suzuki, and cyanation reactions [31–33], as well as for their catalytic activity against the synthesis of 1,2,3-triazoles [34], N-alkylation of amines with alcohols [35], and arylation of heterocyclic C-H bonds [36].

The THPMs-2-oxo-1,2,3,4-tetrahydropyrimidines (Formerly, DH-PMs-3,4-dihydropyrimidin-2(1H)-ones) scaffold is a crucial class of heterocyclic compounds well-known for a wide range of biological activities including anti-HIV [37], anti-tubercular, anti-inflammatory, antibacterial, antioxidant, antifungal [38], and antineoplastic [39] as well as potential therapeutic drugs for a variety of disorders including dia-

* Corresponding authors.

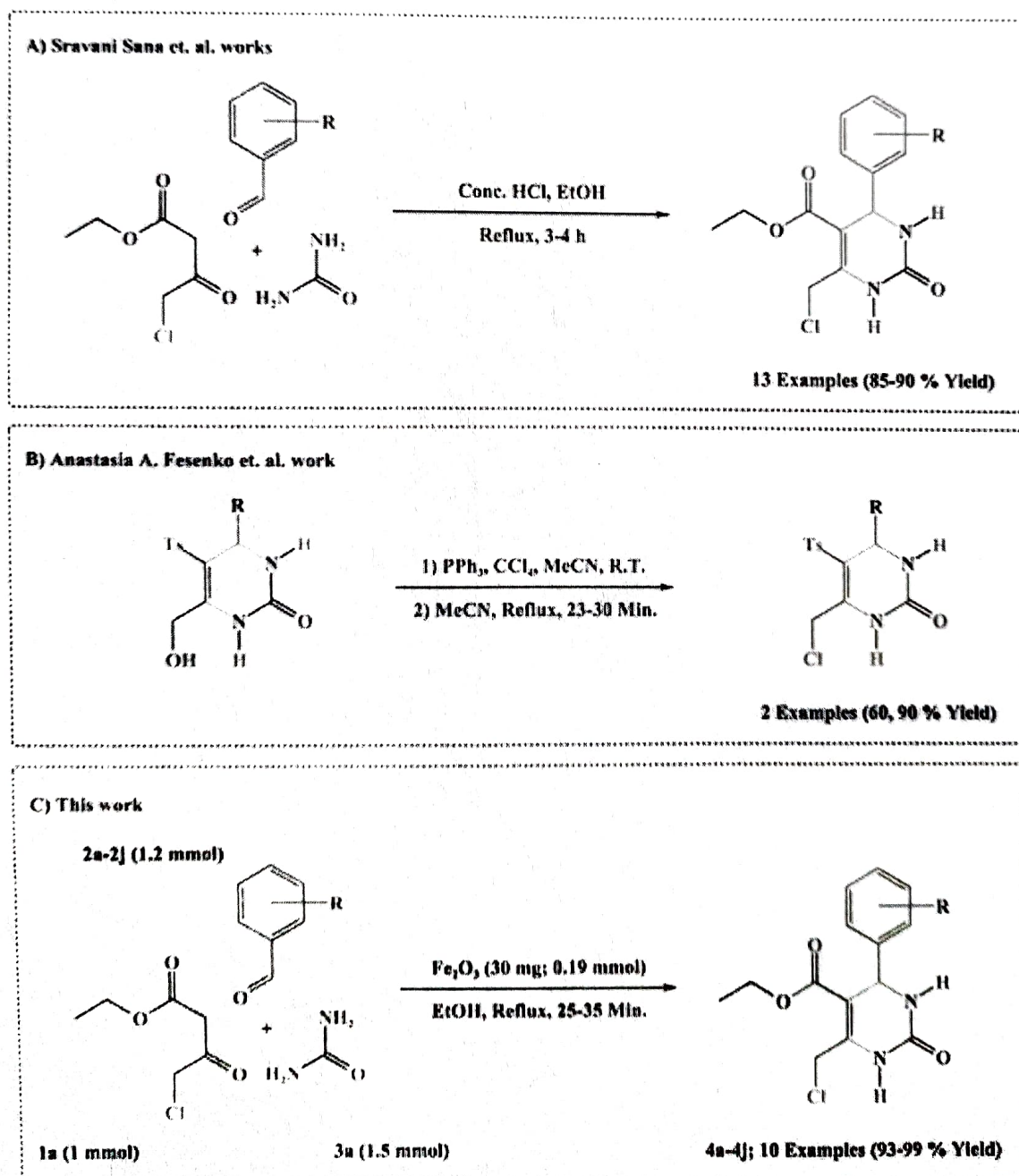
E-mail addresses: sanapdnyanu90258@gmail.com (D. Sanap), ghotekarsuresh7@gmail.com (S. Ghotekar), gaikwad_nd17@yahoo.co.in (N.D. Gaikwad).

betes, Alzheimer's ailment [40,41], and other neuro disorders [39,42]. THPMs are a distinctive framework for building and developing physiologically essential medications and agents for anti-tumor [39] and Alzheimer's disease [40,41] by changing the substituent on its C6 position. 6-(chloromethyl)-THPMs, 6-(bromomethyl)-THPMs, 6-(selenoesters-methyl)-THPMs, 6-(seleno-methyl)-THPMs, 6-(mesyloxymethyl)-THPMs, scaffold is medicinally important and exist in a wide range of biological activities [39–41] as well as the synthetic precursor for new biological active hybrids for anticancer and Alzheimer's disease (e.g., 1,3-Diazepines, Imidazopurines, Pyrimidine core, Spirocyclic core, and Fused core) via substitution and ring expansion reaction [43–47].

Conventionally, the 6-(chloromethyl)-THPMs scaffold was synthesized by the well-known Biginelli reaction by three components reaction between aldehyde, Ethyl 4-chloroacetoacetate, and urea assisted by hydrochloric acid as a homogeneous catalyst [44] with the yield of 72–92 % (Scheme 1a). Anastasia A. Fesenko et al. [47] report the synthesis of 6-(chloromethyl)-THPMs scaffold from 4-(hydroxymethyl)-

THPMs by treatment with the mixture of triphenylphosphine and carbon tetrachloride with the good yield 60–90 % (Scheme 1b). However, there are five major challenges embedded in the synthesis of 6-(chloromethyl)-THPMs scaffold: 1) use of hazardous solvents; 2) use of hazardous reagents; 3) low to moderate yield; 4) long reaction time; 5) recovery of homogenous catalyst. Therefore, there is broad scope for developing a synthetic protocol for the expeditious synthesis of 6-(chloromethyl)-THPMs scaffold to accomplish experimental benevolence, simplicity, sustainability, and effectiveness.

Herein, with this viewpoint in mind, we report the successful synthesis strategy for the 6-(chloromethyl)-THPMs scaffold, using magnetically separable biosynthesized heterogeneous Fe_2O_3 catalyst, with the yield in the range of 93–99 % (Scheme 1c). To the author's knowledge, an entirely green synthesis approach and characterization of the mixed-phase of Fe_2O_3 NRs mediated by the mixture of *Eucalyptus citriodora* and *Murraya koenigii* leaf extract as reducing and stabilizing agents are herein disclosed for the first time. Only a few works have been done to synthesize the NPs using a mixture of different plant leaf extracts.



Scheme 1. Strategies for the construction of ethyl 6-(chloromethyl)-1,2,3,4-tetrahydro-2-oxo-4-arylpyrimidine-5-carboxylate.

Therefore, for this study, we have chosen a mixture of *Eucalyptus citriodora* and *Murraya koenigii* leaf extract for NPs synthesis. Due to the different active phytochemicals of different plant leaves extracts, the rate of NPs formation may be enhanced. Moreover, ^1H NMR and ^{13}C NMR have confirmed the structure of the synthesized Biginelli products.

2. Experimental

2.1. Chemical/ materials

Eucalyptus citriodora leaf (Nilgiri Plant Leaf), *Murraya koenigii* leaf (Curry Leaf), Ferric nitrate nonahydrate ($\text{Fe}(\text{NO}_3)_3 \cdot 9\text{H}_2\text{O}$), substituted aldehydes, ethyl alcohol, ethyl acetate, and n-hexane were purchased from S.D. Fine Chemical Limited. Before being used in this investigation, all the solvents were distilled off.

2.2. Preparation of leaves extracts

The fresh leaves of *Eucalyptus citriodora* and *Murraya koenigii* were collected from the campus of G.M.D. Arts B.W. Commerce and Science College Sinnar, Nashik (Maharashtra), were washed thoroughly with distilled water to remove mud, dirt, impurities, and surface contamination. The wash leaves were weighed accurately at 8 gm each, cut into small pieces and pulverized using the mixer in 10 mL distilled water separately. Transfer the pest to a 100 mL RB flask and add 30 mL of distilled water to each pest mixture, then gently heat at about 80–90 °C for 1 h, then cool it, and filter it with Whatman filter paper (No. 41) [48]. The obtained filtrates use for the synthesis of Fe_2O_3 NRs after mixing.

2.3. Synthesis of Fe_2O_3 NRs

Fe_2O_3 NRs were successfully fabricated by a simple sol-gel auto-combustion technique using the $\text{Fe}(\text{NO}_3)_3 \cdot 9\text{H}_2\text{O}$, *Eucalyptus citriodora*, and *Murraya koenigii* leaves extract precursors.

5 g of $\text{Fe}(\text{NO}_3)_3 \cdot 9\text{H}_2\text{O}$ was dissolved in 15 mL of distilled water, and stir it for the next 30 min at 70–80 °C, to the same homogeneous salt solution, 50 mL of the mixed leaves extract (1:1) added drop by drop over 40 min at 70–80 °C, stirring of mixture was continued for next 30 min upon addition of leaves extract is over. After that, the resulting solution was kept on a hot plate for the next 3 h at about 70–80 °C to get a thick

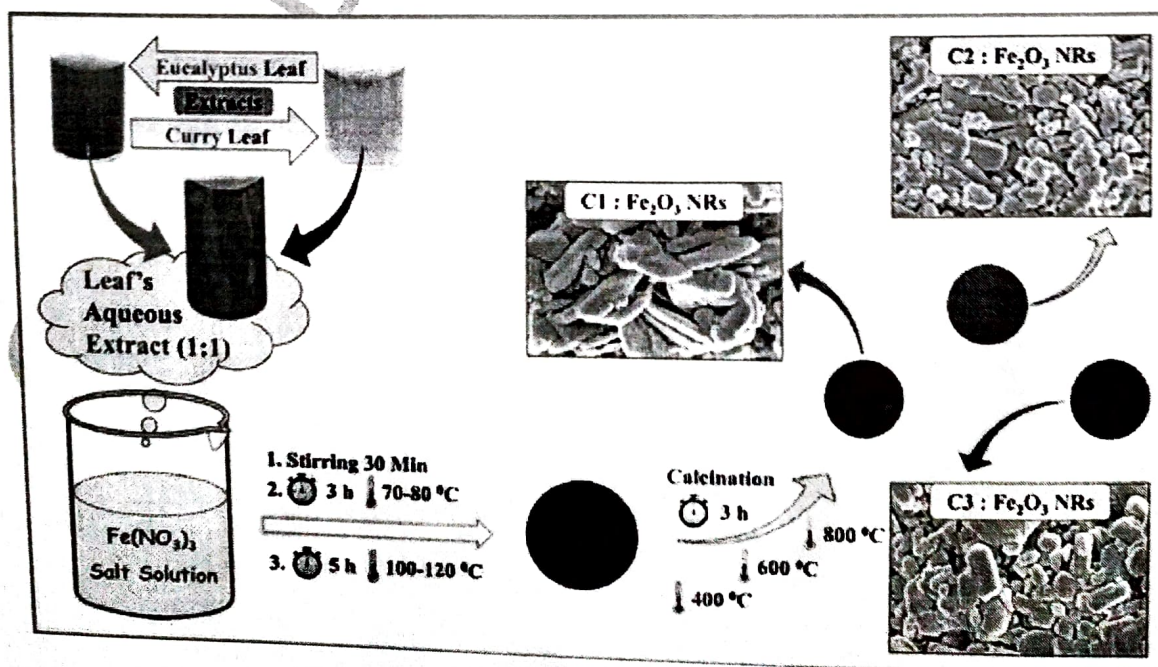
paste. The paste obtained was heated to 100–120 °C for 5 h in a hot air oven for auto-combustion to get a dried thick mass. Further dried mass, grind in mortar-pestle for 30 min to get dry powder. The obtained dried Fe_2O_3 powder was calcinated at three different temperatures via 400 °C, 600 °C, and 800 °C for 3 h. Finally, the dark reddish Brown, Gray, and dark Black Fe_2O_3 powder obtained was named C1 (Fe_2O_3 calcinated at 400 °C), C2 (Fe_2O_3 calcinated at 600 °C), and C3 (Fe_2O_3 calcinated at 800 °C) respectively (Scheme 2). The obtained C1, C2, and C3 nanocrystalline Fe_2O_3 screen for the synthesis of 6-(chloromethyl)-THPMs derivatives.

2.4. General procedure for 6-(chloromethyl)-THPMs synthesis

A mixture of freshly distilled Ethyl 4-chloroacetoacetate (1 mmol), aromatic carbaldehyde (1.2 mmol), Urea (1.5 mmol), and biosynthesized (C1) Fe_2O_3 NRs (0.19 mmol) in ethyl alcohol (3 mL) was well refluxed in a 25 mL RB flask under dark condition (Table No. 7, Entry 1 to 10). TLC was used to track the development of the reaction (using n-Hexane and Ethyl acetate in 1:1 proportion). Upon the completion of the reaction, the reaction mixture is kept near an external magnet for 5 to 7 min to separate the Fe_2O_3 catalyst, and then the ethanolic layer of the reaction mixture is separated by decanting into a beaker through Whatman filter paper. In the end, the catalyst in RB was washed using 1 mL ethanol every time thrice, dried, activated, and used for a sequential cycle. After column chromatography, the pure product was obtained using n-hexane and ethyl acetate (85:15 to 40:60) solvent as a mobile phase. By using ^1H NMR, and ^{13}C NMR techniques, all the organic products were confirmed.

2.5. C1, C2 and C3 sample characterization technique

Model V-770 - Jasco Spectrophotometer was used to get a UV-DRS of Fe_2O_3 NRs. The UV-DRS absorption spectra were measured from 200 to 800 nm. A JASCO-4600, Type-A model spectrophotometer was used to acquire FT-IR spectra of NRs in the 400 to 4000 cm^{-1} range. Bruker D8 diffractometer having Cu-K α radiation (having $\lambda = 1.54060 \text{ \AA}$) with an angle between 20° to 80°, with a minimum step size of 2 θ is 0.020° were carried out for crystal structure analysis of biosynthesized NRs. 10 kV accelerating voltage FEI Nova Nano SEM 450 instrument was used to examine cross-section morphology or surface structure and



Scheme 2. Schematic diagram describing the synthesis of Fe_2O_3 NRs.

element mapping of NRs. Quanta-Chrome NOVA 1000e model instrument was used to acquire the data of N_2 adsorption-desorption, pore-size distribution, and pore diameter at 77 K. The magnetic behavior of biosynthesized NRs was investigated using Vibrating Sample Magnetometry. Thiele's tube assembly measured the melting points of the synthesized 6-(chloromethyl)-THPMs scaffold. Finally, the Bruker Advance NEO 500 MHz Spectrometer was used to confirm the molecular structure of synthesized Ethyl 6-(chloromethyl)-THPMs scaffold with the instrument strength of 500 MHz and 126 MHz for 1H and ^{13}C nuclei, respectively.

3. Result and discussion

3.1. Physical, chemical, and structural characterization of the catalyst

The powder X-Ray Diffraction pattern of biosynthesized Fe_2O_3 (C1, C2, and C3) demonstrates that all the sample contains Hematite and Maghemite mixed phase, with rhombohedral and cubic crystal systems, respectively [49]. Fig. 1 revealed characteristic X-Ray Diffraction peaks at 2θ : 24.18 (110), 33.20 (211), 35.68 (101), 40.92 (210), 49.53 (202), 54.15 (312), 64.10 (211), 72.01 (433), and 26.18 (211), 30.23 (202), 35.72 (311), 43.42 (400), 46.20 (411), 57.44 (511), 63.01 (404), 74.66 (533) for Hematite and Maghemite phase respectively. This result of the mixed phase is in good agreement with previous studies for Hematite [50,51] and Maghemite [52], respectively. The average crystalline size of mixed-phase biosynthesized NRs was calculated using Scherrer's equation by Full Width at Half Maximum (FWHM) for prominent peaks, which were found to be 18.36, 24.48, and 65.79 nm for C1, C2, and C3 samples respectively (Table 1).

Further morphological characteristics, sizes, and element mapping of fabricated Fe_2O_3 NRs were studied by FESEM analysis, as shown in Fig. 2. According to FESEM images, the rod-shaped morphology and uniform distribution were obtained for C1 (a-b), C2 (e-f), and C3 (i-j) as-prepared NRs, and distribution of Iron (Fe) and Oxygen (O) elements in Bio-fabricated Fe_2O_3 material were studied by element mapping C1 (c-d), C2 (g-h) and C3 (k-l), respectively.

Additionally, as demonstrated in Fig. 3, the EDX spectrum indicated the Fe_2O_3 NRs elemental composition for C1 (Fig. 3a), C2 (Fig. 3b), and

C3 (Fig. 3c) samples. This EDX analysis (Fig. 3d) shows that the material contains Iron (Fe) and Oxygen (O), demonstrating the formation of Fe_2O_3 NRs.

The FTIR spectrum was used to investigate the nature of chemical bonding in the molecule. Fig. 4, FTIR spectrum of biosynthesized Fe_2O_3 NRs, shows intense absorption peaks at 1581, 1095, 594, and 532 cm^{-1} . The peak at 1581 cm^{-1} may correspond to the amide bending vibration of proteins N-H bond or may be due to the stretching vibration of aromatic C=C bonds [53]. The next observed peaks at 1095 cm^{-1} could be caused by aliphatic ether C-O stretching [53]. The two strong peaks of stretching vibration at 594 and 532 cm^{-1} correspond to Fe-O bond formation in Fe_2O_3 - C1, C2, and C3 samples [54,55].

Fig. 5 illustrates the main active phytochemicals found in *Eucalyptus citriodora* (Fig. 5a), and *Murraya koenigii* (Fig. 5b) leaves to explain how the metal precursor salt $Fe(NO_3)_2 \cdot 9H_2O$ can change into Fe_2O_3 nanorods. The plausible reaction mechanism demonstrates how different active phytochemicals act as stabilizing and reducing agents. Diverse active phytochemicals are found in *Eucalyptus citriodora* and *Murraya koenigii* leaves, including saponins, carbohydrates, sterols, glycosides, alkaloids, flavonoids, terpenoids, and polyphenols [56–58]. For a possible reaction mechanism, a flavonoid has been chosen as a sample molecule to suggest the mechanism. Because of the electrostatic attraction between hydroxyl groups of flavonoid and cation of metal precursor, aromatic hydroxyl groups cling to ferric ions (Fe^{3+}), and ferric ions and flavonoids form a stable complex. After the treatment of calcination, the complex decomposes and forms Fe_2O_3 nanorods. As a result, the single-phase formation of Fe_2O_3 is not selective. Therefore, two phases were observed in the XRD analysis corresponding to α - Fe_2O_3 and γ - Fe_2O_3 (Fig. 6).

The optical absorbance of the fabricated C1, C2, and C3 mixed-phase Fe_2O_3 NRs (α - Fe_2O_3 -Hematite and γ - Fe_2O_3 -Maghemite) was investigated in the range of 200 to 800 nm [59]. The corresponding spectrum is shown in Fig. 7a. The absorption spectra of a C1, C2, and C3- Fe_2O_3 NRs show the presence of three distinct adsorption zones [60], namely, the first region (200–400 nm) due to charge-transfer from ligands to Fe^{3+} metal ion and because of the Fe^{3+} ligand field transitions contributions, in part from $^6A_1 \rightarrow ^4T_1(^4P)$ at 290–310 nm, $^6A_1 \rightarrow ^4E(^4D)$ and $^6A_1 \rightarrow ^4T_2(^4D)$ at 360–380 nm. The second region (400–600 nm)

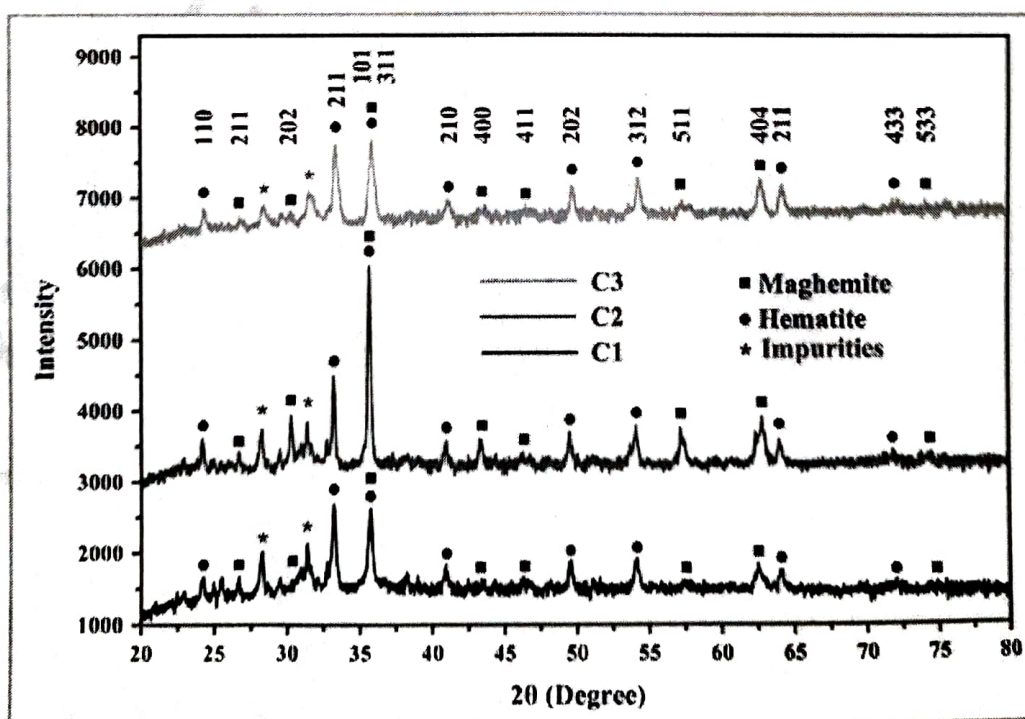


Fig. 1. XRD patterns of biosynthesized Fe_2O_3 NRs, calcined at (C1) 400 °C, (C2) 600 °C and (C3) 800 °C.

Table 1
Calculation of average crystal size of biosynthesized Fe_2O_3 NRs by Scherer equation using FWHM for listed prominent peaks.

Sample	2 θ (Degree)	FWHM	Crystalline Size D (nm)	Average D (nm)		
C1	24.20	4.5012	1.74	18.36		
	33.20	0.3323	24.12			
	35.70	0.3734	21.61			
	40.91	0.3421	23.96			
	49.53	0.3521	24.02			
	54.12	0.4462	19.33			
	62.97	0.7046	12.76			
	64.10	0.4688	19.33			
	C2	24.17	0.2336		34.79	28.48
		33.18	0.2417		34.29	
35.71		0.2772	30.10			
40.90		0.2969	28.55			
43.37		0.2988	28.61			
49.51		0.3114	28.09			
54.14		0.5161	17.28			
57.41		0.4408	20.54			
62.95		0.2507	37.06			
64.07		0.3672	25.52			
C3	24.21	0.4084	17.91	65.79		
	33.31	0.4121	18.11			
	35.71	0.4382	17.15			
	41.02	0.3837	19.90			
	49.65	0.0199	395.24			
	54.31	0.4065	19.77			
	62.98	0.4556	18.38			
	64.13	0.4252	19.86			

represents the end consequence of pair excitation of processes ${}^6A_1 + {}^6A_1 \rightarrow {}^4T_1({}^4G) + {}^4T_1({}^4G)$ at 485–550 nm and overlapped contribution of ${}^6A_1 \rightarrow {}^4E$, ${}^4A_1({}^4G)$ ligand field transitions at 430 nm and the charge-transfer band tail. Region third (600–750 nm) is attributed to 640 nm for the ${}^6A_1 \rightarrow {}^4T_2({}^4G)$ transition. Furthermore, according to the selection rules, the area's first and second absorption intensity is significantly higher than that of the third region, indicating that the absorption from charge-transfer transitions or pair excitations is much stronger than that from ligand field transitions [61]. The bandgap energy of biosynthesized Fe_2O_3 NRs is calculated using Tauc's plot (direct method) (Fig. 7b-d) and was estimated to be 2.02, 1.98, and 1.79 eV for C1, C2, and C3 samples, respectively.

Surface area and porosity of Fe_2O_3 NRs were calculated by Brunauer-Emmett-Teller (BET) N_2 adsorption/desorption studies to get an idea of the absorbance capacity of biosynthesized Fe_2O_3 NRs, and Pore Size distribution (PSD) was obtained by Barrett-Joyner-Halenda (BJH) plot (Fig. 8). The surface area of the as-formulated C1 sample was observed to be $16.13 \text{ m}^2 \text{ g}^{-1}$ which is almost 5 and 48 times higher than the as-prepared C2 ($3.2097 \text{ m}^2 \text{ g}^{-1}$) and C3 ($0.33738 \text{ m}^2 \text{ g}^{-1}$) samples respectively (Table 2). Similarly, the prepared samples' pore volume and diameter were found to decrease and increase with rising in calcination temperature, respectively (Table 2).

The magnetic behavior of biosynthesized Fe_2O_3 NRs was investigated by Vibrating Sample Magnetometry (VSM). Fig. 9 shows the hysteresis loop for synthesized Fe_2O_3 NRs. The value of M_s , H_c , and M_r (Table 3) were estimated based on the hysteresis loop by applying the applied field in the range of -15 kOe to 15 kOe to study the magnetic characteristics of NRs.

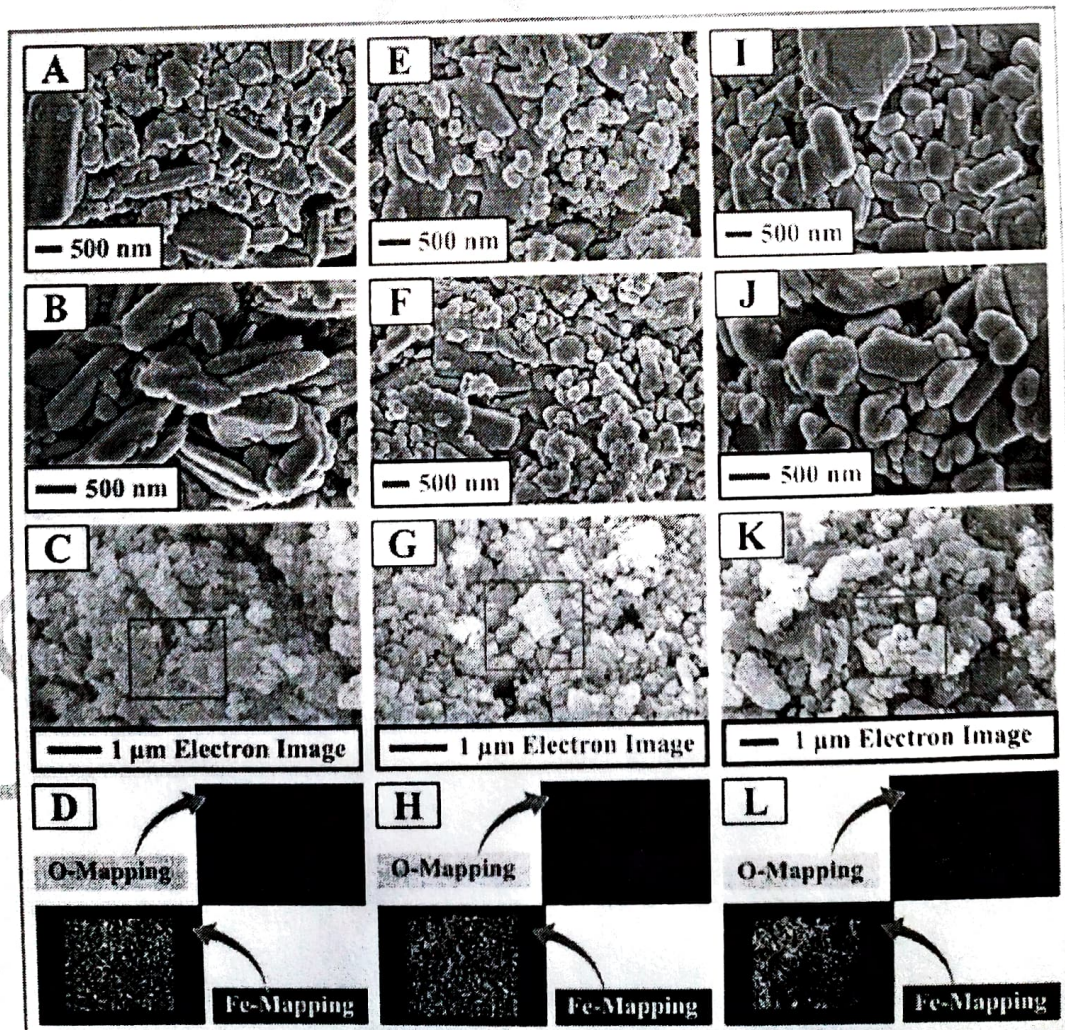


Fig. 2. FE-SEM images of as-prepared Fe_2O_3 NRs; C1 (a-b), C2 (e-f) and C3 (i-j) and element mapping of synthesized NRs C1 (c-d), C2 (g-h) and C3 (k-l).

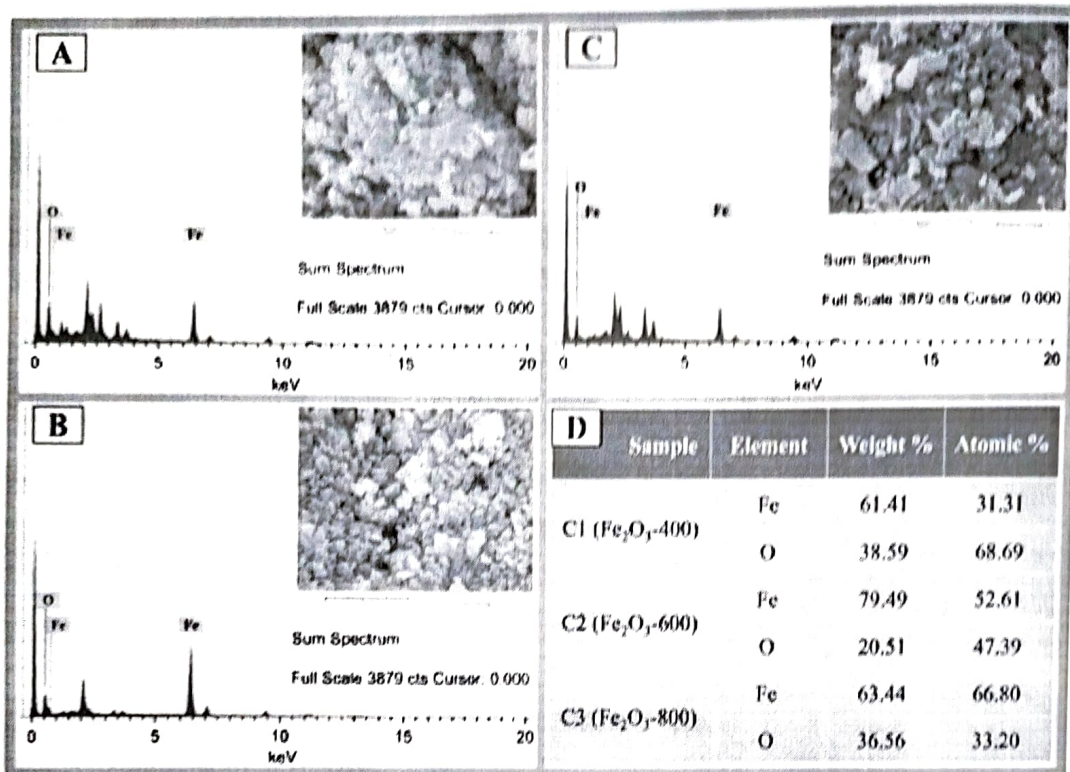


Fig. 3. EDX spectrum of synthesized C1, C2, and C3 - Fe₂O₃ NRs (a-c); Percent element composition of C1, C2, and C3 - Fe₂O₃ NRs (d).

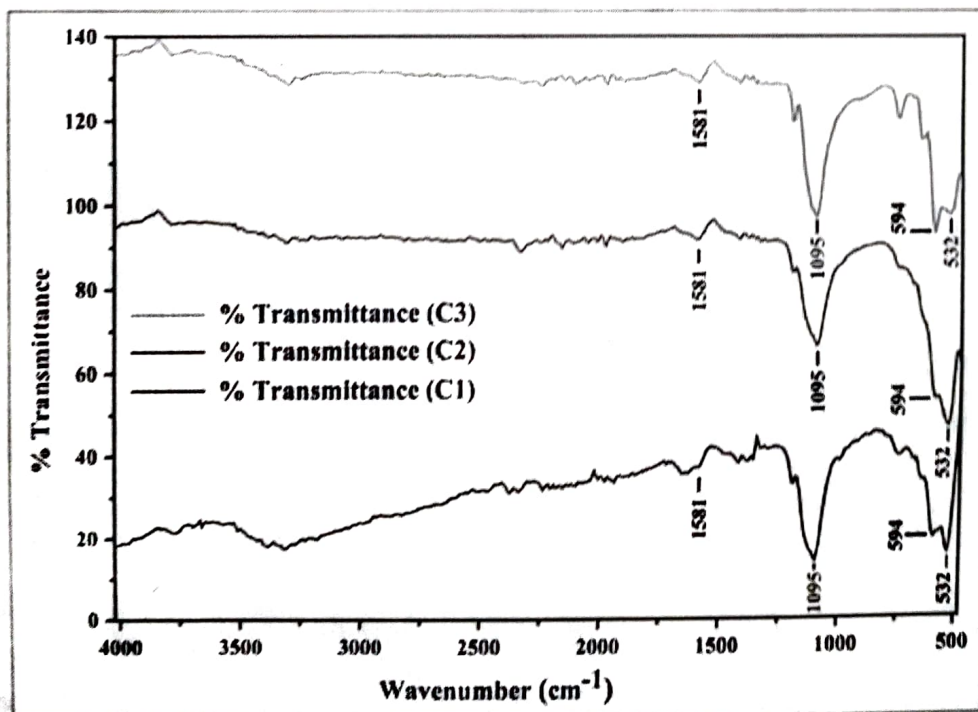


Fig. 4. FTIR spectrum of biosynthesized Fe₂O₃ NRs, calcined at (C1) 400 °C, (C2) 600 °C and (C3) 800 °C.

3.2. Optimization of reaction condition for the synthesis of Ethyl 6-(chloromethyl)-1,2,3,4-tetrahydro-2-oxo-4-phenyl pyrimidine-5-carboxylate (4a)

We investigated the Fe₂O₃ (C1, C2, and C3) heterogeneous catalyst for 6-(chloromethyl)-1,2,3,4-tetrahydro-2-pyrimidinone derivatives

synthesis using freshly distilled Ethyl 4-chloroacetoacetate (1a) with benzaldehyde (2a), and Urea (3a) into corresponding Ethyl 6-(chloromethyl)-1,2,3,4-tetrahydro-2-oxo-4-phenyl pyrimidine-5-carboxylate (4a) in the presence of ethyl alcohol (3 mL) as a solvent under the refluxing condition in the dark.

Under refluxing conditions, C1, C2, and C3 heterogeneous catalysts (10 mg; 0.06 mmol; 1.67 mol %) were investigated for 6-

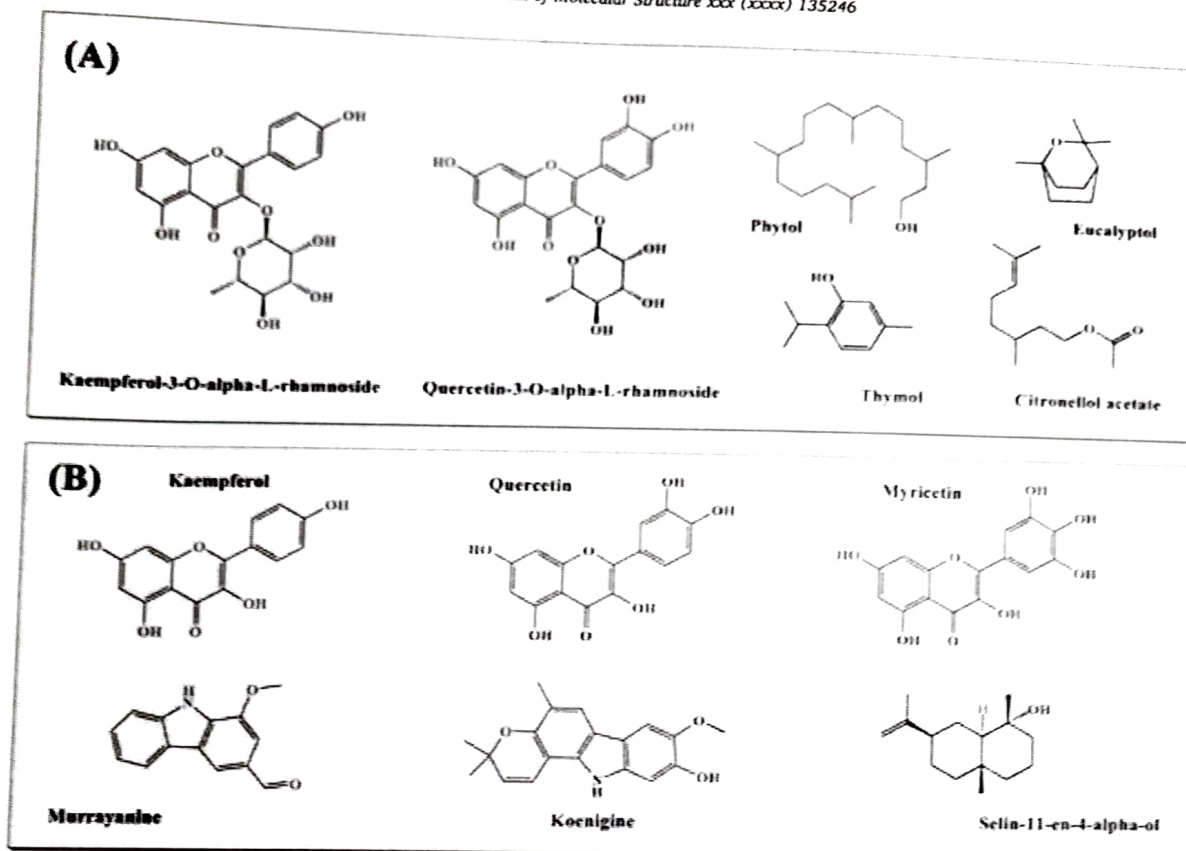


Fig. 5. Biologically active phytochemicals present in a) *Eucalyptus citriodora* and b) *Murraya koenigii* leaves.

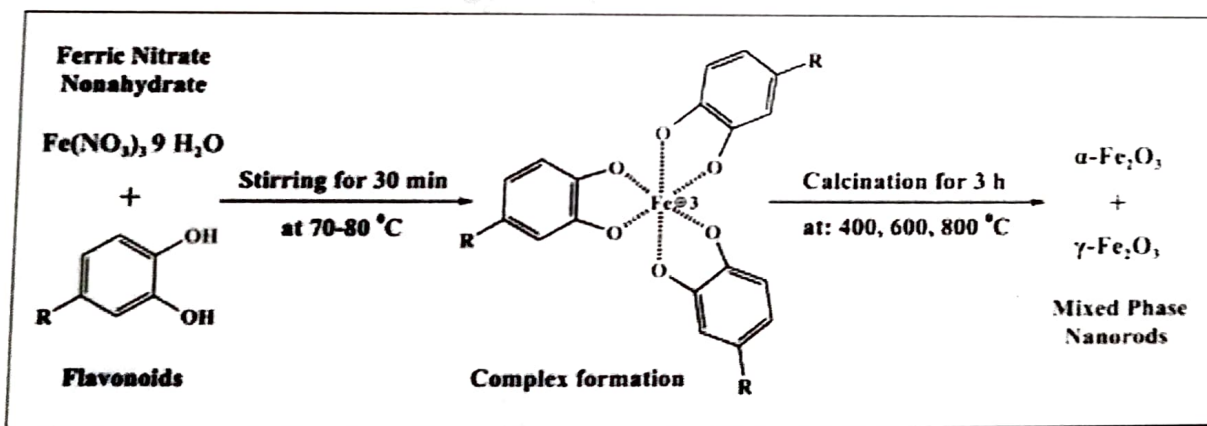


Fig. 6. A plausible reaction mechanism for the formation of Fe_2O_3 NRs using metal salt and leaf extracts.

(chloromethyl)-1,2,3,4-tetrahydro-2-pyrimidinone derivatives synthesis using Ethyl 4-chloroacetoacetate 1a (1 mmol) with benzaldehyde 2a (1.2 mmol) and Urea 3a (1.5 mmol). Table 4, Entry 1–7 summarises the yields of 4a for employing sundry Fe_2O_3 potential heterogeneous catalysts.

Further, benzaldehyde (2a) and urea (3a) mole fractions were optimized for the model 6-(chloromethyl)-1,2,3,4-tetrahydro-2-pyrimidinone derivatives synthesis from Ethyl 4-chloroacetoacetate 1a (1 mmol) using C1 (Fe_2O_3 NRs; 10 mg; 0.06 mmol) as a potential catalyst for Biginelli reaction. The highest yield of 4a (43 %) was observed for 1.2 mmol of benzaldehyde with 1.5 mmol of urea within 30 min under the refluxing condition in ethyl alcohol (Table 5, Entry 9).

The catalytic amount of Fe_2O_3 (C1) was screened in optimal circumstances (1a 1 mmol, 2a 1.2 mmol, 3a 1.5 mmol, and ethyl alcohol as solvent under refluxing condition) and got the highest yield of 4a (99 %) within 30 min for 30 mg (0.19 mmol; 4.8 mol %) of catalyst (Table 6, Entry 6). Spectra data of synthesized compounds are as follows:

3.2.1. Ethyl 6-(chloromethyl)-1,2,3,4-tetrahydro-2-oxo-4-phenylpyrimidine-5-carboxylate (4a)

^1H NMR (500 MHz, DMSO) δ : 9.50 (d, $J = 2.1$ Hz, 1H), 7.86 (dd, $J = 3.4, 2.1$ Hz, 1H), 7.36–7.32 (m, 2H), 7.28–7.24 (m, 3H), 5.19 (d, $J = 3.4$ Hz, 1H), 4.78 (d, $J = 10.6$ Hz, 1H), 4.59 (d, $J = 10.6$ Hz, 1H), 4.06–4.01 (q, $J = 7.1$ Hz, 2H), 1.11 (t, $J = 7.1$ Hz, 3H), 3.35 (s, H_2O Residue), 2.50 (p, DMSO Residue); ^{13}C NMR (126 MHz, DMSO) δ : 164.67, 152.49, 146.49, 144.42, 129.01, 128.06, 126.76, 102.23, 60.43, 54.36, 39.67, 14.34, 39.98 (DMSO Residue).

3.2.2. Ethyl 6-(chloromethyl)-4-(4-fluorophenyl)-1,2,3,4-tetrahydro-2-oxopyrimidine-5-carboxylate (4b)

^1H NMR (500 MHz, DMSO) δ : 9.53 (d, $J = 0.8$ Hz, 1H), 7.86 (m, 1H), 7.31–7.27 (m, 2H), 7.20–7.15 (m, 2H), 5.21 (d, $J = 3.3$ Hz, 1H), 4.78 (d, $J = 10.6$ Hz, 1H), 4.60 (d, $J = 10.6$ Hz, 1H), 4.04 (t, $J = 7.1$ Hz, 2H), 1.11 (t, $J = 7.1$ Hz, 3H), 3.37 (s, H_2O Residue), 2.50 (p, DMSO Residue), 1.91 (s, AcOH Residue); ^{13}C NMR (126 MHz,

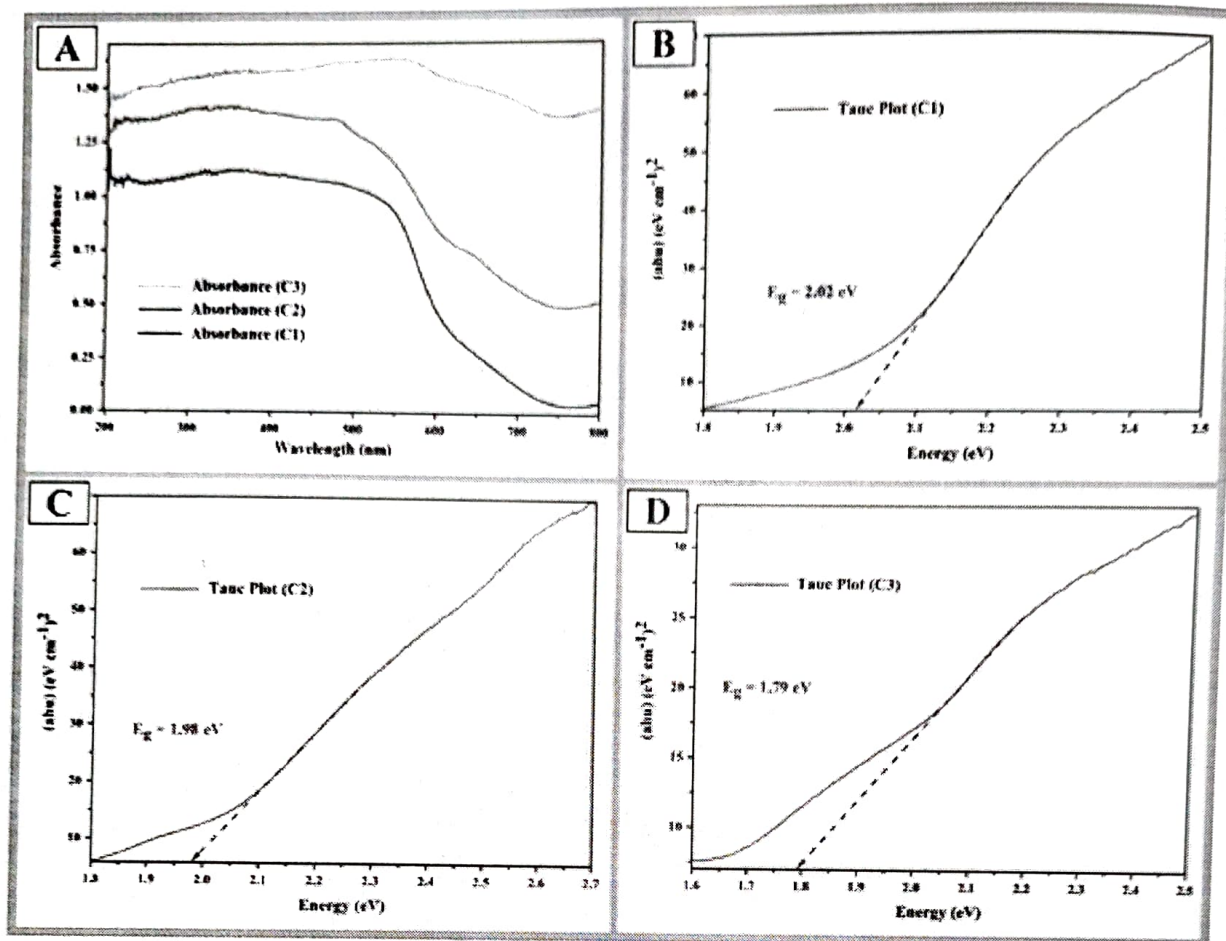


Fig. 7. a) UV-DRS spectrum of bio-synthesized C1, C2, and C3 - Fe_2O_3 NRs; Band-gap energy by Tauc Plot C1(b), C2(c), and C3(d).

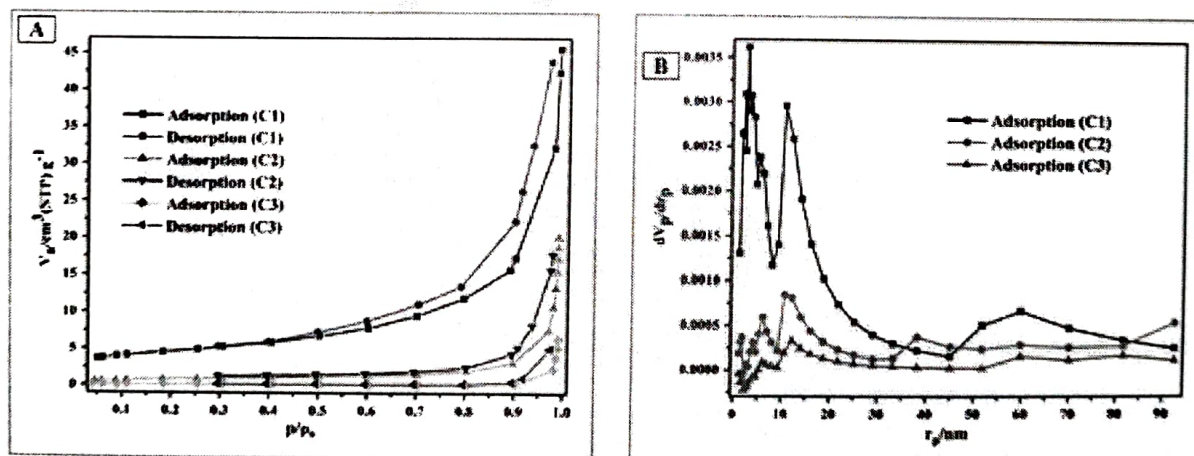


Fig. 8. a) Nitrogen adsorption-desorption isotherms at -196°C , calcined at (C1) 400°C , (C2) 600°C and (C3) 800°C (BET plot); b) Pore size distribution plot of Fe_2O_3 NRs calcined at (C1) 400°C , (C2) 600°C and (C3) 800°C (BJH plot).

Table 2

Summary for N_2 adsorption/ desorption, pore size distribution and pore volume for biosynthesized Fe_2O_3 catalyst.

Sample Code & Name	Surface area (BET) ($\text{m}^2 \text{g}^{-1}$)	Pore volume (BJH) ($\text{cm}^3 \text{g}^{-1}$)	Pore diameter (BJH) (nm)
C1- Fe_2O_3 NRs	16.130	0.0695800	17.254
C2- Fe_2O_3 NRs	3.2097	0.0303570	37.832
C3- Fe_2O_3 NRs	0.3374	0.0092712	109.92

DMSO) δ : 164.57, 161.96 (d, $J = 243.5$ Hz), 152.34, 146.65, 140.70 (d, $J = 3.0$ Hz), 128.80 (d, $J = 8.3$ Hz), 115.77 (d, $J = 21.4$ Hz), 102.06, 60.46, 53.71, 39.61, 14.33, 39.96 (DMSO Residue), AcOH Residue: 172.50, 21.50.

3.2.3. Ethyl 6-(chloromethyl)-4-(4-chlorophenyl)-1,2,3,4-tetrahydro-2-oxypyrimidine-5-carboxylate (4c)

^1H NMR (500 MHz, DMSO) δ : 9.55 (d, $J = 1.0$ Hz, 1H), 7.88 (m, 1H), 7.42 (d, $J = 8.5$ Hz, 2H), 7.27 (d, $J = 8.5$ Hz, 2H), 5.20 (d, $J = 3.3$ Hz, 1H), 4.78 (d, $J = 10.6$ Hz, 1H), 4.58 (d, $J = 10.6$ Hz, 1H), 4.05 (q, $J = 7.1$ Hz, 2H), 1.12 (t, $J = 7.1$ Hz, 3H), 3.34 (s, H_2O Residue), 2.50 (p, DMSO Residue); ^{13}C NMR (126 MHz, DMSO) δ : 164.53, 152.31, 146.84,

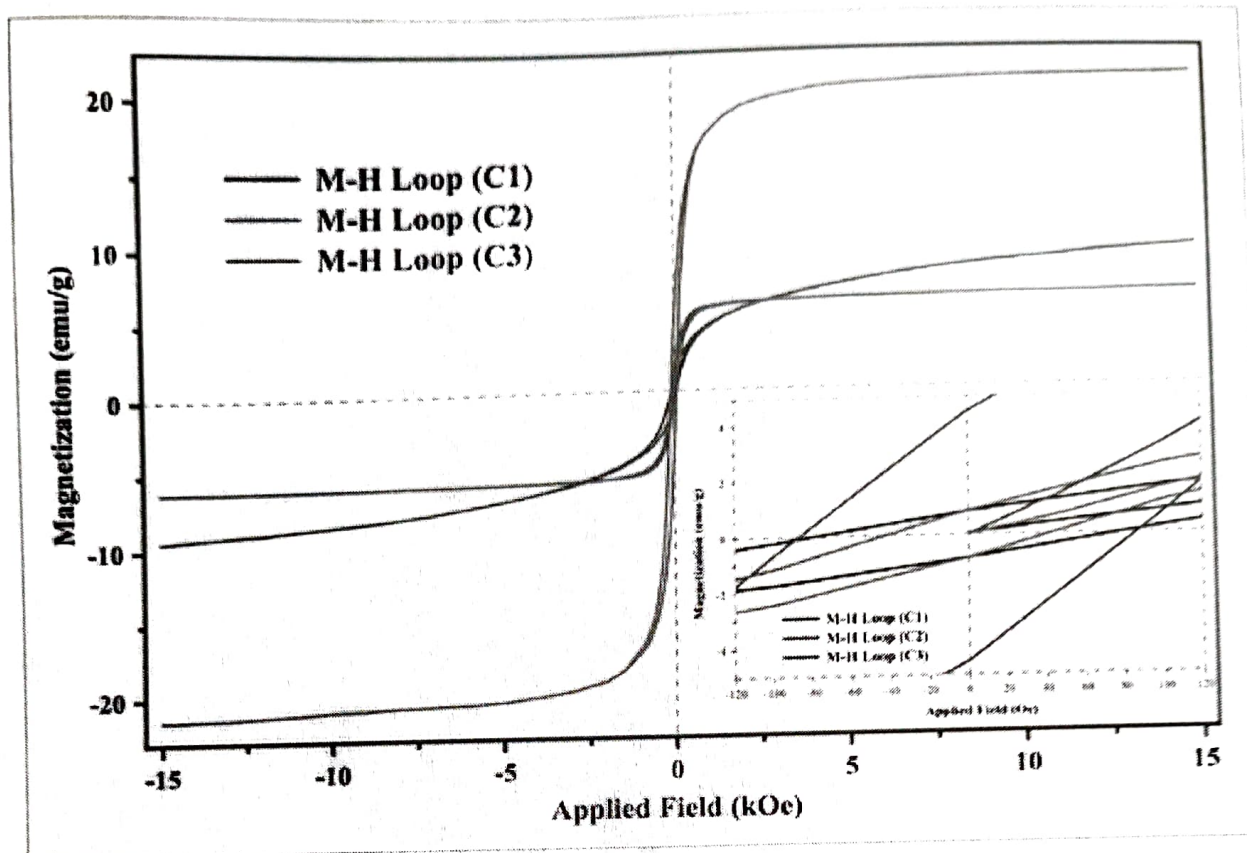


Fig. 9. VSM plot, calcined at (C1) 400 °C, (C2) 600 °C and (C3) 800 °C.

Table 3
Summary for Magnetic properties of biosynthesized Fe₂O₃ NRs.

Sample Code & Name	Saturation magnetization (Ms)	Coercivity (Hc)	Remnant field (Mr)
C1-Fe ₂ O ₃ NRs	09.39 emu g ⁻¹	78.98 Oe	0.84 emu g ⁻¹
C2-Fe ₂ O ₃ NRs	21.16 emu g ⁻¹	86.98 Oe	4.44 emu g ⁻¹
C3-Fe ₂ O ₃ NRs	06.37 emu g ⁻¹	42.35 Oe	0.85 emu g ⁻¹

143.36, 132.62, 129.02, 128.69, 101.76, 60.50, 53.79, 39.82, 14.34, 39.98 (DMSO Residue).

3.2.4. Ethyl 4-(4-bromophenyl)-6-(chloromethyl)-1,2,3,4-tetrahydro-2-oxopyrimidine-5-carboxylate (4d)

¹H NMR (500 MHz, DMSO) δ: 9.55 (d, *J* = 1.5 Hz, 1H), 7.88 (dd, *J* = 3.0, 2.1 Hz, 1H), 7.57–7.54 (m, 2H), 7.23–7.20 (m, 2H), 5.18 (d, *J* = 3.3 Hz, 1H), 4.78 (d, *J* = 10.6 Hz, 1H), 4.58 (d, *J* = 10.6 Hz, 1H), 4.04 (q, *J* = 7.1 Hz, 2H), 1.12 (t, *J* = 7.1 Hz, 3H), 3.34 (s, H₂O Residue), 2.50 (p, DMSO Residue); ¹³C NMR (126 MHz, DMSO) δ: 164.52, 152.30, 146.85, 143.77, 131.95, 129.04, 121.16, 101.70, 60.51, 53.86, 39.65, 14.35, 39.99 (DMSO Residue).

3.2.5. Ethyl 6-(chloromethyl)-4-(2-fluorophenyl)-1,2,3,4-tetrahydro-2-oxopyrimidine-5-carboxylate (4e)

¹H NMR (500 MHz, DMSO) δ: 9.56 (s, 1H), 7.82 (s, 1H), 7.35–7.28 (m, 2H), 7.20–7.15 (m, 2H), 5.50 (d, *J* = 3.0 Hz, 1H), 4.77 (d, *J* = 10.6 Hz, 1H), 4.64 (d, *J* = 10.6 Hz, 1H), 3.98 (q, *J* = 7.1 Hz, 2H), 1.06 (t, *J* = 7.1 Hz, 3H), 3.34 (s, H₂O Residue), 2.50 (p, DMSO Residue); ¹³C NMR (126 MHz, DMSO) δ: 164.36, 159.76 (d, *J* = 247.0 Hz), 151.95, 147.10, 131.32 (d, *J* = 13.7 Hz), 130.20 (d, *J* = 8.3 Hz), 129.20 (d, *J* = 3.9 Hz), 125.09 (d, *J* = 3.2 Hz), 116.02 (d, *J* = 21.9 Hz), 100.48, 60.34, 48.98 (d, *J* = 3.3 Hz), 39.54, 14.16, 39.97 (DMSO Residue).

3.2.6. Ethyl 4-(2-bromophenyl)-6-(chloromethyl)-1,2,3,4-tetrahydro-2-oxopyrimidine-5-carboxylate (4f)

¹H NMR (500 MHz, DMSO) δ: 9.39 (d, *J* = 4.1 Hz, 1H), 7.72 (bs, 1H), 7.05 (d, *J* = 8.2 Hz, 2H), 6.70 (d, *J* = 8.2 Hz, 2H), 5.09 (d, *J* = 2.5 Hz, 1H), 4.77 (d, *J* = 10.6 Hz, 1H), 4.58 (d, *J* = 10.6 Hz, 1H), 4.03 (q, *J* = 7.0 Hz, 2H), 1.12 (t, *J* = 7.0 Hz, 3H), 3.36 (s, H₂O Residue), 2.50 (p, DMSO Residue); ¹³C NMR (126 MHz, DMSO) δ: 164.76, 157.28, 152.53, 145.87, 134.97, 127.96, 115.59, 102.74, 60.35, 53.85, 39.73, 14.38, 39.96 (DMSO Residue).

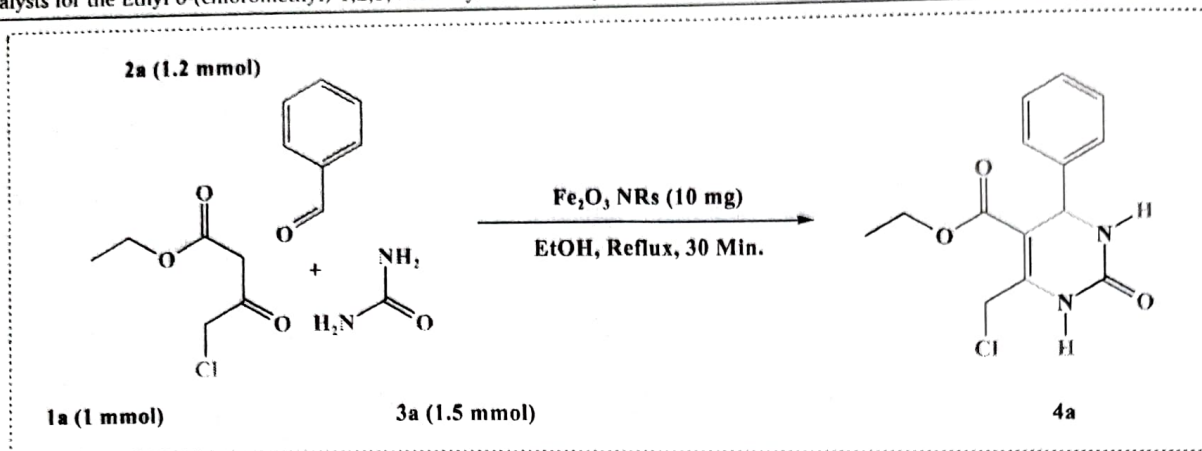
3.2.7. Ethyl 6-(chloromethyl)-1,2,3,4-tetrahydro-4-(4-hydroxyphenyl)-2-oxopyrimidine-5-carboxylate (4g)

¹H NMR (500 MHz, DMSO) δ: 9.58 (d, *J* = 1.2 Hz, 1H), 7.85–7.83 (m, 1H), 7.60 (dd, *J* = 8.0, 1.0 Hz, 1H), 7.40–7.33 (m, 2H), 7.21 (ddd, *J* = 8.0, 7.0, 2.0 Hz, 1H), 5.67 (d, *J* = 3.0 Hz, 1H), 4.77 (d, *J* = 10.6 Hz, 1H), 4.70 (d, *J* = 10.6 Hz, 1H), 3.96 (q, *J* = 7.1 Hz, 2H), 1.02 (t, *J* = 7.1 Hz, 3H), 3.33 (s, H₂O Residue), 2.50 (p, DMSO Residue); ¹³C NMR (126 MHz, DMSO) δ: 164.31, 151.65, 147.42, 143.11, 133.23, 130.16, 129.08, 129.00, 122.76, 101.23, 60.31, 54.31, 39.53, 14.29, 39.99 (DMSO Residue).

3.2.8. Ethyl 6-(chloromethyl)-1,2,3,4-tetrahydro-4-(2-hydroxyphenyl)-2-oxopyrimidine-5-carboxylate (4h)

¹H NMR (500 MHz, DMSO) δ: 7.79 (s, 1H), 7.48 (d, *J* = 4.3 Hz, 1H), 7.25–7.22 (m, 2H), 6.97 (td, *J* = 7.5, 1.0 Hz, 1H), 6.88–6.86 (m, 1H), 4.59 (dd, *J* = 4.3, 3.3 Hz, 1H), 4.35 (d, *J* = 11.7 Hz, 1H), 4.21 (q, *J* = 7.1 Hz, 2H), 3.98 (d, *J* = 11.7 Hz, 1H), 3.42–3.40 (m, 1H), 1.24 (t, *J* = 7.1 Hz, 3H), 3.34 (s, H₂O Residue), 2.50 (p, DMSO Residue); ¹³C NMR (126 MHz, DMSO) δ: 168.31, 154.53, 150.58, 130.09, 129.30, 125.34, 121.65, 117.25, 84.57, 61.45, 47.97, 46.80, 41.34, 14.43, 39.98 (DMSO Residue).

Table 4
Screening of catalysts for the Ethyl 6-(chloromethyl)-1,2,3,4-tetrahydro-2-oxo-4-phenylpyrimidine-5-carboxylate synthesis.

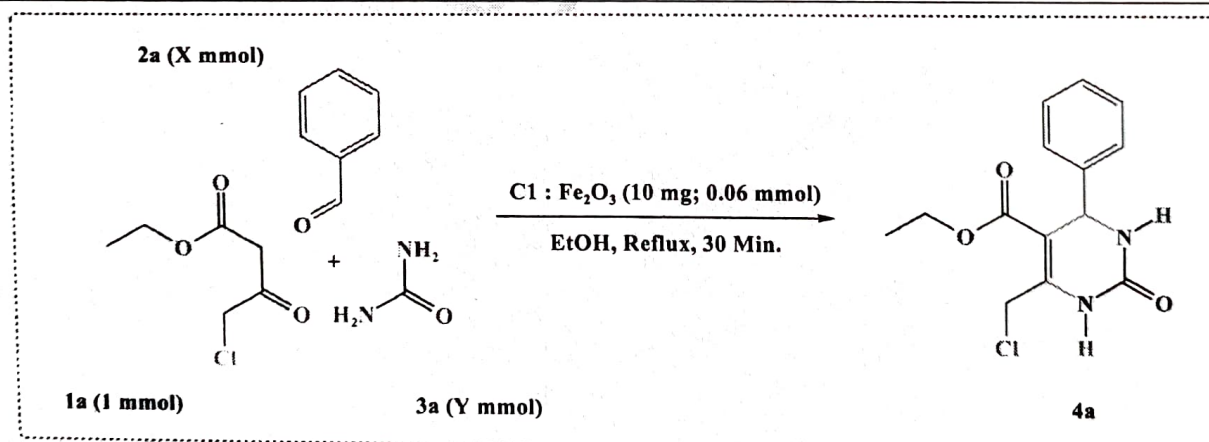


Entry ^a	Catalyst	Time (Min.)	4a-Yield (%) ^b
1	Blank	30	Tress amount
2	C1-Catalyst	30	43
3	C2-Catalyst	30	36
4	C3-Catalyst	30	22
5	C1-Catalyst	60	55
6	C2-Catalyst	60	49
7	C3-Catalyst	60	38

^a Reaction Condition: Ethyl 4-chloroacetoacetate (1 mmol), Benzaldehyde (1.2 mmol), Urea (1.5 mmol), Ethanol (3 mL), Catalyst (10 mg; 0.06 mmol; 1.67 mol %) under refluxing condition.

^b Isolated yield.

Table 5
Screening of mole fraction of benzaldehyde and urea for Ethyl 6-(chloromethyl)-1,2,3,4-tetrahydro-2-oxo-4-phenylpyrimidine-5-carboxylate synthesis.



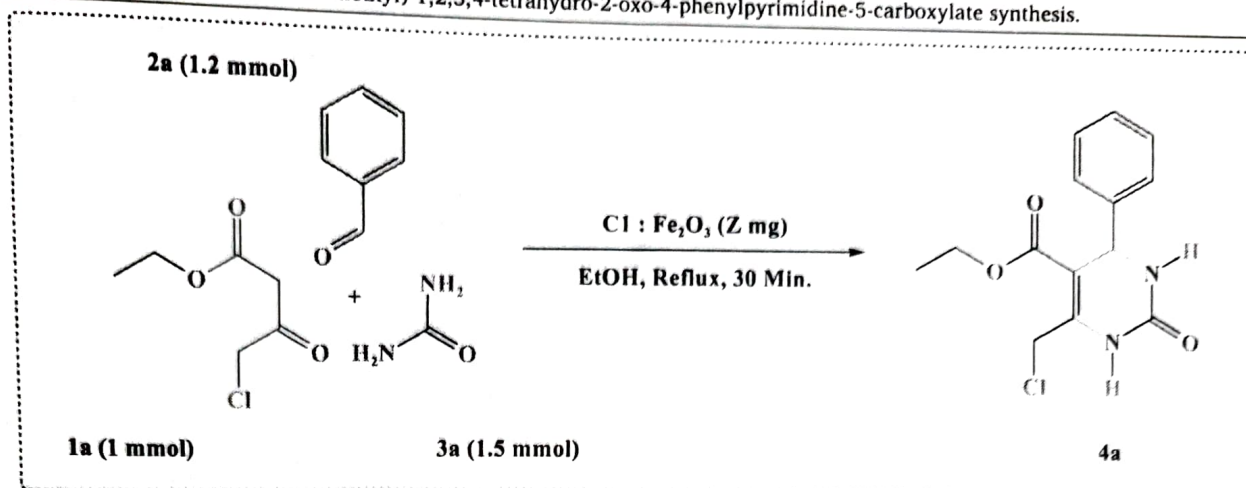
Entry ^a	Benzaldehyde 2a (X mmol)	Urea 3a (Y mmol)	Yield (4a %) ^b
1	1.0	1.1	25
2	1.0	1.3	25
3	1.0	1.5	28
4	1.0	1.7	27
5	1.1	1.3	32
6	1.1	1.5	40
7	1.1	1.7	40
8	1.2	1.3	39
9	1.2	1.5	43
10	1.2	1.7	43
11	1.3	1.5	43
12	1.3	1.7	42

^a Reaction Condition Ethyl 4-chloroacetoacetate (1 mmol), Benzaldehyde, Urea, Solvent (3 ml), Catalyst C1-NRs (10 mg; 0.06 mmol; 1.67 mol %) under reflux condition for 30 min.

^b Isolated yield.

Table 6

Screening of catalytic amount for Ethyl 6-(chloromethyl)-1,2,3,4-tetrahydro-2-oxo-4-phenylpyrimidine-5-carboxylate synthesis.



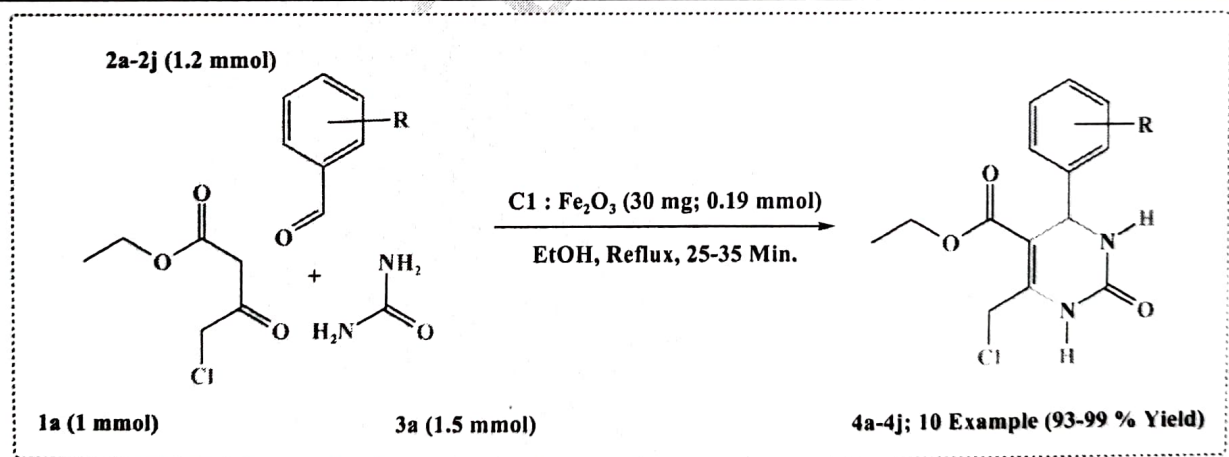
Entry ^a	Catalyst amount (Z mg)	4a-Yield (%) ^b
1	5	19
2	10	30
3	15	43
4	20	61
5	25	83
6	30	99
7	35	99

^a Reaction Condition: Ethyl 4-chloroacetate (1 mmol), Benzaldehyde (1.2 mmol), Urea (1.5 mmol), Solvent (3 mL), Catalyst-Cl-Fe₂O₃ NRs (Z mg) under reflux condition for 30 min.

^b Isolated yield.

Table 7

Fe₂O₃-Cl catalyzed synthesis of Ethyl 6-(chloromethyl)-1,2,3,4-tetrahydro-2-oxo-4-arylpyrimidine-5-carboxylate (4a-4j) using Ethyl 4-chloroacetate (1a) with aromatic aldehyde (2a-2j) and Urea (3a).



Entry ^a	Aryl Carbaldehyde	Product	Time (Min)	Yield (%) ^b	MP (°C)	Ref.
1	Phenyl	4a	30	99	193	[39,41-42]
2	4-Fluoro Phenyl	4b	25	99	190	New
3	4-Chloro Phenyl	4c	27	98	191	[39,42]
4	4-Bromo Phenyl	4d	30	98	183	[42]
5	2-fluoro Phenyl	4e	35	97	241	New
6	2-Bromo Phenyl	4f	35	95	227	New
7	4-Hydroxy Phenyl	4g	35	96	175	New
8	2-Hydroxy Phenyl	4h	35	93	274	New
9	4-Methoxy Phenyl	4i	35	94	213	[41-42]
10	2-Methoxy Phenyl	4j	35	97	182	[42]

^a Reaction Condition: Ethyl 4-chloroacetate (1 mmol), Aromatic aldehyde (1.2 mmol), Urea (1.5 mmol), Ethanol (3 ml), Catalyst-(Cl)-Fe₂O₃ NRs (30 mg; 0.19 mmol; 4.83 mol %) under reflux condition.

^b Isolable yield.

Study of Recovery & Reusability of Biosynthesized Fe₂O₃ NRs

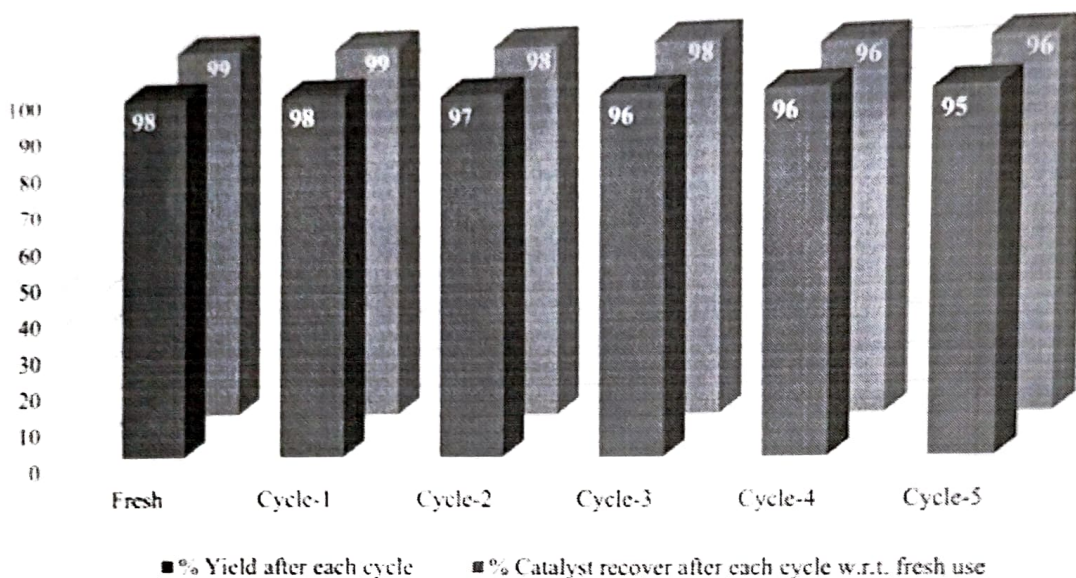


Fig. 10. Study of recovery and reusability of biosynthesized Fe₂O₃ NRs heterogeneous catalyst for the synthesis of ethyl 6-(chloromethyl)-1,2,3,4-tetrahydro-2-oxo-4-phenylpyrimidine-5-carboxylate under standard conditions shown in Table 7 (Entry 1).

3.2.9. Ethyl 6-(chloromethyl)-1,2,3,4-tetrahydro-4-(4-methoxyphenyl)-2-oxopyrimidine-5-carboxylate (4i)

¹H NMR (500 MHz, DMSO) δ: 9.45 (s, 1H), 7.78 (bs, 1H), 7.17 (d, *J* = 8.6 Hz, 2H), 6.89 (d, *J* = 8.6 Hz, 2H), 5.14 (d, *J* = 3.0 Hz, 1H), 4.76 (d, *J* = 10.6 Hz, 1H), 4.60 (d, *J* = 10.6 Hz, 1H), 4.04 (q, *J* = 7.0 Hz, 2H), 3.72 (s, 3H), 1.12 (t, *J* = 7.0 Hz, 3H), 3.34 (s, H₂O Residue), 2.50 (p, DMSO Residue); ¹³C NMR (126 MHz, DMSO) δ: 164.71, 159.14, 152.51, 146.14, 136.58, 127.95, 114.32, 102.53, 60.39, 55.54, 53.74, 39.72, 14.37, 39.97 (DMSO Residue).

3.2.10. Ethyl 6-(chloromethyl)-1,2,3,4-tetrahydro-4-(2-methoxyphenyl)-2-oxopyrimidine-5-carboxylate (4j)

¹H NMR (500 MHz, DMSO) δ: 9.39 (bs, 1H), 7.43 (bs, 1H), 7.27–7.23 (m, 1H), 7.11 (dd, *J* = 7.3, 1.3 Hz, 1H), 7.00 (d, *J* = 8.1 Hz, 1H), 6.88 (t, *J* = 7.3 Hz, 1H), 5.52 (d, *J* = 3.0 Hz, 1H), 4.75 (d, *J* = 10.6 Hz, 1H), 4.66 (d, *J* = 10.6 Hz, 1H), 3.98 (q, *J* = 7.1 Hz, 2H), 3.79 (s, 3H), 1.05 (t, *J* = 7.1 Hz, 3H), 3.33 (s, H₂O Residue), 2.50 (p, DMSO Residue); ¹³C NMR (126 MHz, DMSO) δ: 164.74, 157.02, 152.58, 146.82, 131.32, 129.46, 127.70, 120.62, 111.67, 100.86, 60.20, 55.80, 49.59, 39.65, 14.29, 39.98 (DMSO Residue).

3.3. Study of recovery and reusability of biosynthesized Fe₂O₃ NRs

The recovered catalyst was washed using 1 mL ethanol every time thrice after completion of the reaction, afterward dried at 150 °C for 2 h in a hot air oven, further activating the same NRs at 350 °C for 2 h in a muffle furnace after every reuse for use in consecutive cycles. Interestingly, the biosynthesized Fe₂O₃ NRs (C1) catalytic activity was not affected when reused five times. Fig. 10 shows the graphical representation for recovery and a corresponding yield of 4a for each cycle of Fe₂O₃ NRs (C1) use.

3.4. Probable mechanistic pathway of the reaction

Various theoretical and experimental discussions have been reported for the mechanistic pathway of the Biginelli reaction. The three mechanistic pathways have been proposed based on the intermediate involved in the reaction (Fig. 11).

The first mechanistic path is the iminium route (Fig. 11a) [62], which involves condensation of aldehyde and urea to get iminium intermediate, on which nucleophilic addition of ethyl 4-chloro-3-hydroxybut-2-enoate (enol generated in-situ form Ethyl 4-chloroacetoacetate) leads to the formation of 6-(chloromethyl)-THPMs. The second mechanistic path is via the enamine route (Fig. 11b) [63]. It involves condensation of β-keto ester and urea leads to protonated enamine intermediate, which subsequently undergoes nucleophilic addition on aldehyde to get 6-(chloromethyl)-THPMs. The third mechanistic path involves a Knoevenagel-type reaction (Fig. 11c) [64]. Here firstly, the condensation of an aldehyde with ethyl 4-chloro-3-hydroxybut-2-enoate (enol generated in-situ form Ethyl 4-chloroacetoacetate) takes place, which on reaction with urea result in the formation of 6-(chloromethyl)-THPMs.

In the last decade, De Souza et al. [65], Neto et al. [66], and Puripat et al. [67] did a comparative study on the mechanistic path of the Biginelli reaction. They found that the Iminium intermediate route is favored over the Enamine and Knoevenagel route. According to Puripat et al. [67], based on AFIR and DFT calculation, the order of reactive intermediate formation is Imine > Enamine > Knoevenagel route.

4. Conclusion

In this study, for the first time, mixed-phase Fe₂O₃ NRs were biologically synthesized using a mixture of Eucalyptus citriodora and Murraya koenigii leaf extracts and its application as a heterogeneous magnetic nanocatalyst in the multicomponent Biginelli reaction was reported. The catalyst was synthesized through an utterly green approach and then characterized by XRD, UVDRS, FTIR, FESEM, EDX, and VSM analysis. Then, the practical synthesis of 6-(chloromethyl)-1,2,3,4-tetrahydro-2-pyrimidinone derivatives (4a-4j) was prepared with an ethyl 4-chloroacetoacetate, several aromatic aldehydes, urea with a catalytic amount of the magnetically recoverable Fe₂O₃ NRs in ethanol as a green solvent. The notable merits of this protocol are easy workup procedure, reusability of catalyst, being clean and safe, and having excellent yields of the final products. This eco-friendly approach for synthesizing Fe₂O₃ NRs can open new horizons for exploring their possible role in organic transformation.

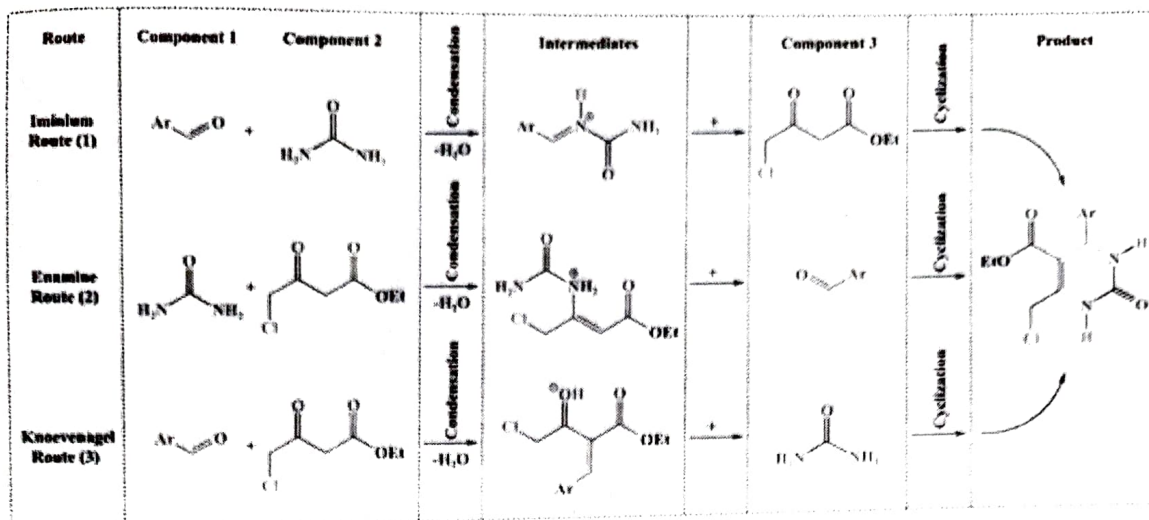


Fig. 11. Possible reaction mechanism for the Fe₂O₃ NRs catalyzed 6-(chloromethyl)-THPMs synthesis.

Declaration of Competing Interest

The authors declare that they have no known competing financial interests or personal relationships that could have appeared to influence the work reported in this paper.

Data Availability

Data will be made available on request.

Acknowledgement

We thank CIF (Central Instrumentation Facilities), Savitribai Phule Pune University, Pune, for UV-DRS, FTIR, BET, XRD, FE-SEM, EDX, 1H NMR, and ¹³C NMR analysis.

Supplementary materials

Supplementary material associated with this article can be found, in the online version, at doi:10.1016/j.molstruc.2023.135246.

References

- [1] S.D. Roy, K.C. Das, S.S. Dhar, Conventional to green synthesis of magnetic iron oxide nanoparticles; its application as catalyst, photocatalyst and toxicity: a short review, *Inorg. Chem. Commun.* 134 (2021) 109050.
- [2] S. Asiya, et al., Sustainable preparation of gold nanoparticles via green chemistry approach for biogenic applications, *Mater. Today Chem.* 17 (2020) 100327.
- [3] A. Barhoum, et al., A broad family of carbon nanomaterials: classification, properties, synthesis, and emerging applications. *Handbook of Nanofibers*, 2019, pp. 1–40.
- [4] K. Pal, et al., A critical review on multifunctional smart materials 'nanographene' emerging avenue: nano-imaging and biosensor applications, *Crit. Rev. Solid State Mater. Sci.* 47 (5) (2022) 691–707.
- [5] H.N. Cuong, et al., New frontiers in the plant extract mediated biosynthesis of copper oxide (CuO) nanoparticles and their potential applications: a review, *Environ. Res.* 203 (2022) 111858.
- [6] C.W. Wong, et al., Response surface methodology optimization of mono-dispersed MgO nanoparticles fabricated by ultrasonic-assisted sol-gel method for outstanding antimicrobial and antibiofilm activities, *J. Cluster Sci.* 31 (2020) 367–389.
- [7] K. Pal, et al., Cutting edge development on graphene derivatives modified by liquid crystal and CdS/TiO₂ hybrid matrix: optoelectronics and biotechnological aspects, *Crit. Rev. Solid State Mater. Sci.* 46 (5) (2021) 385–449.
- [8] A.C. Suwarno, et al., Biosynthesis of Dy₂O₃ nanoparticles using Piper Retrofractum Vahl extract: optical, structural, morphological, and photocatalytic properties, *J. Mol. Struct.* 1264 (2022) 133123.
- [9] I. Halomoan, et al., Facile preparation of CuO-Gd₂Ti₂O₇ using Aemella uliginosa leaf extract for photocatalytic degradation of malachite green, *Mater. Res. Bull.* 150 (2022) 111726.
- [10] D.O.B. Apriandanu, Y. Yulizar, CuO-bentonite-gold nanocomposites: facile green preparation and their characterization, *Mater. Lett.* 284 (2021) 128911.
- [11] D.O.B. Apriandanu, Y. Yulizar, Tinospora crista leaves extract for the simple preparation method of CuO nanoparticles and its characterization, *Nano-Struct. Nano-Objects* 20 (2019) 100401.
- [12] S. Pansambal, et al., Bioengineered cerium oxide (CeO₂) nanoparticles and their diverse applications: a review, *Appl. Nanosci.* (2022) 1–26.
- [13] S. Pansambal, et al., Recent developments on magnetically separable ferri-ter-based nanomaterials for removal of environmental pollutants, *J. Nanomater.* (2022) 2022.
- [14] A. Indriyani, et al., One-pot green fabrication of BiFeO₃ nanoparticles via Abelmoschus esculentus L. leaves extracts for photocatalytic dye degradation, *Appl. Surf. Sci.* 563 (2021) 150113.
- [15] Y. Yulizar, D.O.B. Apriandanu, J.L. Al Jabbar, Facile one-pot preparation of V₂O₅-Fe₂O₃ nanocomposites using Foeniculum vulgare extracts and their catalytic property, *Inorg. Chem. Commun.* 123 (2021) 108320.
- [16] K. Mishra, N. Basavegowda, Y.R. Lee, Biosynthesis of Fe, Pd, and Fe-Pd bimetallic nanoparticles and their application as recyclable catalysis for [3 + 2] cycloaddition reaction: a comparative approach, *Catal. Sci. Technol.* 5 (5) (2015) 2612–2621.
- [17] L. Voss, et al., The presence of iron oxide nanoparticles in the food pigment E172, *Food Chem.* 327 (2020) 127000.
- [18] K. Qiao, et al., Application of magnetic adsorbents based on iron oxide nanoparticles for oil spill remediation: a review, *J. Taiwan Inst. Chem. Eng.* 97 (2019) 227–236.
- [19] N.V. Long, et al., Iron oxide nanoparticles for next generation gas sensors, *Int. J. Metall. Mater. Eng.* 1 (1) (2015) 1–18.
- [20] Y. Tuo, et al., Microbial synthesis of Pd/Fe₃O₄, Au/Fe₃O₄ and PdAu/Fe₃O₄ nanocomposites for catalytic reduction of nitroaromatic compounds, *Sci. Rep.* 5 (1) (2015) 13515.
- [21] A. Rostami-Vartooni, et al., Biosynthesis and catalytic activity of Pd/NiFe₂O₄ nanocomposite for the reduction of wastewater pollutants, *Nanochem. Res.* 6 (2) (2021) 248–255.
- [22] A. Rostami-Vartooni, A. Moradi-Saadatmand, M. Mahdavi, Catalytic reduction of organic pollutants using biosynthesized Ag/C/Fe₃O₄ nanocomposite by red water and Caesalpinia gilliesii flower extract, *Mater. Chem. Phys.* 219 (2018) 328–339.
- [23] S. Pansambal, et al., Efficient synthesis of magnetically separable CoFe₂O₄@SiO₂ nanoparticles and its potent catalytic applications for the synthesis of 5-aryl-1, 2, 4-triazolidine-3-thione derivatives, *J. Water Environ. Nanotechnol.* 4 (3) (2019) 174–186.
- [24] S. Bucak, B. Yavuztürk, A.D. Sezer, Magnetic nanoparticles: synthesis, surface modifications and application in drug delivery, *Recent Adv. Novel Drug Carrier Syst.* 2 (2012) 165–200.
- [25] S. Naz, et al., Green synthesis of hematite (α-Fe₂O₃) nanoparticles using Rhus punjabensis extract and their biomedical prospect in pathogenic diseases and cancer, *J. Mol. Struct.* 1185 (2019) 1–7.
- [26] S. Shylesh, V. Schünemann, W.R. Thiel, Magnetically separable nanocatalysts: bridges between homogeneous and heterogeneous catalysis, *Angew. Chem. Int. Ed.* 49 (20) (2010) 3428–3459.
- [27] D. Sanap, et al., An expedient synthesis of C3-arylidene-oxindole derivatives using calcite nanoflowers as an efficient heterogeneous catalyst, *Inorg. Chem. Commun.* (2023) 110387.
- [28] G. Kaur, et al., Magnetically separable transition metal ferrites: versatile heterogeneous nano catalysts for the synthesis of diverse bioactive heterocycles, *ChemistrySelect* 4 (7) (2019) 2181–2199.
- [29] H. Dabhaee, et al., MgO nanoparticles: synthesis, characterization, and applications as a catalyst for organic transformations, *Eur. J. Chem.* 12 (1) (2021) 86–108.
- [30] S. Sobhani, Z. Pakdin-Parizi, Palladium-DABCO complex supported on γ-Fe₂O₃ magnetic nanoparticles: a new catalyst for CC bond formation via Mizoroki-Heck cross-coupling reaction, *Appl. Catal. A* 479 (2014) 112–120.